JOURNAL OF AIRCRAFT
Vol. 31, No. 6, November–December 1994

Navier-Stokes Prediction of Large-Amplitude Delta-Wing Roll Oscillations

Neal M. Chaderjian*
NASA Ames Research Center, Moffett Field, California 94035

Vortical flow about a 65-deg sweep delta wing at 15-deg angle of attack is numerically simulated for static roll and forced roll oscillations using the time-dependent, three-dimensional, Reynolds-averaged, Navier-Stokes (RANS) equations. This is a first step towards the development of an experimentally validated computational method for simulating wing rock with the RANS equations. Turbulent computations are presented for static roll angles up through 42 deg. The effects of roll angle on the vortex aerodynamics are discussed, and solution accuracy is evaluated by comparison with experimental data. The effects of grid refinement and zonal boundary condition treatment are assessed at zero roll angle. Computational results for a large-amplitude (Φ_{max} = 40 deg), high-rate (f = 7 Hz) forced roll motion is also presented. Computed static and dynamic surface-pressure coefficients, rolling-moment coefficients, normal-force coefficients, and streamwise c.p. locations compare very well with experimental data. The static rolling-moment coefficients indicate the wing is statically stable under the present flow conditions. Moreover, the dynamic rolling-moment coefficients indicate that the fluid extracts energy from the wing motion, i.e., the wing is positively damped. The computed and experimental damping energy agree within 3%.

Introduction

THERE is considerable interest to fly modern tactical fighters at high angles of attack. This "high-alpha" flight regime is rich in complex fluid phenomena, e.g., streamwise and crossflow separation, vortex asymmetry, and vortex breakdown, which are inherently nonlinear and often time-dependent. Strong vortical flow structures exist that provide additional nonlinear lift, and can be exploited to provide improved aircraft maneuverability and agility. Although certain performance gains can be realized in the high-alpha regime, the vortices themselves can produce some adverse side affects. For example, vortex asymmetries interacting with an aircraft's motion can lead to wing rock,[1] a sustained periodic motion in roll and yaw. This dynamic condition can result in departure from controlled flight.

Experimental investigations aimed at understanding the wing rock phenomenon have been carried out on simplified delta-wing geometries with a single degree of freedom (DOF) in roll. This avoids the complexity of complete aircraft geometries while focusing on the relevant flow physics. Experimental data typically consist of flow visualization and time-dependent forces and moments.[2–6] More recently, experimental investigations have included time-dependent surface-pressure data.[7–11]

Computational fluid dynamics (CFD) has just begun to be utilized to investigate and predict wing rock motions. These computations provide greater flowfield detail than is otherwise available or possible with experiment alone, and therefore compliment the experimental data. The numerical prediction of wing rock, however, can require large amounts of computer time. In order to offset the computational cost, Lee and Batina[12] and Kandil and Salman[13] have simplified their computations by using the inviscid Euler equations, together with the conical flow assumption. More recently, Kandil and Salman[14] used the three-dimensional Euler equations.

The inviscid and conical flow approximations do improve the computational efficiency, but cannot model some of the physical mechanisms associated with wing rock. For example, the conical approximation reduces the three-dimensional physical flow into a two-dimensional computation using similarity principles. This prevents vortex breakdown, which often accompanies wing rock. Moreover, the inviscid approximation cannot account for vortices that are known to form on smooth surfaces, e.g., an aircraft's forebody, secondary, and tertiary vortices. The strength of an inviscid vortex may also be incorrect. This could affect the position of vortex breakdown, as well as the resulting forces and moments that drive wing rock motions. Methods based on these approximations will have limited utility in realistic aircraft applications.

The approach adopted here is to utilize the three-dimensional, time-dependent, Reynolds-averaged, Navier-Stokes (RANS) equations. The RANS approach requires more computer time, but contains all of the relevant flow physics. The Navier-Stokes Simulation (NSS) code is used to simulate vortical flow about a 65-deg sweep delta wing at 15-deg angle of attack. Static (fixed) roll angles and a large-amplitude, high-rate roll oscillation are presented. These computations are a first step towards the development of an experimentally validated computational method for the eventual prediction and analysis of wing rock using the RANS equations.

A description of the experiment used to validate the computations is given in the next section. This is followed by a discussion of the governing equations, turbulence model, numerical algorithm, computational grids, and boundary conditions. Computational results are then presented and compared with detailed experimental data. Finally, concluding remarks are presented.

Summary of Wind-Tunnel Experiment

Extensive wind-tunnel investigations for a 65-deg leading-edge sweep delta wing were carried out by Hanff et al.[7–10] at the Institute for Aerospace Research (IAR) in Ottawa, Canada, and the Air Force Wright Aeronautical Laboratory (AFWAL). A three-view drawing of the delta wing is shown

Presented as Paper 92-4428 at the AIAA Atmospheric Flight Mechanics Conference, Hilton Head Island, SC, Aug. 10–12, 1992; received Nov. 19, 1992; revision received March 15, 1994; accepted for publication March 18, 1994.

*Research Scientist, Applied Computational Fluids Branch. Senior Member AIAA.

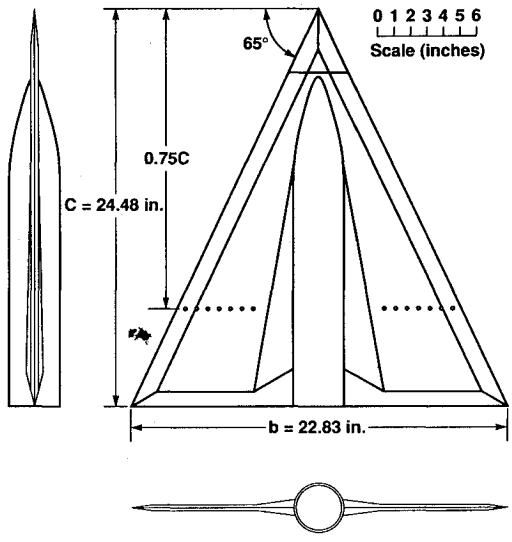

Fig. 1 Three-view drawing of the delta-wing model.

in Fig. 1. The delta wing is symmetric from top to bottom and from side to side. Bevels run parallel along the leading and trailing edges of the model. The delta wing is mounted on a fuselage/sting that contains instrumentation and allows for a single DOF in roll. The fuselage has a tangent-ogive cylinder shape and the sting has a reduced diameter aft of the wing trailing edge. Bevels join the fuselage to the flat wing surface for additional stiffness. The model is constructed of a multilayer carbon-composite skin and foam core, resulting in a stiff, lightweight model having a low rolling moment of inertia. Dynamic pressure transducers are located across the span of the wing on the upper surface at 75% of the root chord.

Very high-quality experimental data was obtained in the form of static and dynamic surface pressures, forces, and moments. A laser light sheet technique was used to visualize the off-body vortices, and an oil flow technique was used to visualize surface-flow patterns. The experiment was conducted by Hanff et al.[7-9] in the IAR 6- × 9-ft low-speed wind tunnel and the 7- × 10-ft AFWAL Subsonic Aerodynamic Research Laboratory (SARL) tunnel.[10] The SARL data was used throughout this article. Additional details about the experiment, including an extensive test matrix, can be found in the cited references.

Numerical Approach

Governing Equations

The time-dependent RANS equations are transformed from Cartesian coordinates (x, y, z, t) to body-fitted curvilinear coordinates (ξ, η, ζ, τ) to simplify the implementation of boundary conditions. The thin-layer approximation is also used, where it is assumed that viscous terms are most significant in the body-normal ζ-coordinate direction. This is consistent with the high Reynolds number flows investigated below. The RANS equations can therefore be expressed in the following strong conservation-law form:

$$\partial_\tau \hat{Q} + \partial_\xi \hat{E} + \partial_\eta \hat{F} + \partial_\zeta \hat{G} = Re^{-1} \partial_\zeta \hat{S} \qquad (1)$$

where $\hat{Q}$ is the vector of conserved dependent variables, $\hat{E}$, $\hat{F}$, and $\hat{G}$ are the inviscid flux vectors in the ξ, η, and ζ directions, respectively, and $\hat{S}$ is the thin-layer viscous flux vector. These equations have been nondimensionalized by the wing root chord C, and the freestream speed of sound a_∞. Any body movement or grid deformation is accommodated through coordinate transformation metrics that are included in the flux vectors. The perfect gas law, Sutherland's viscosity law, and a turbulence model completes the RANS system of equations. Further details of Eq. (1) can be found in Ref. 15.

Turbulence Model

The Baldwin-Lomax algebraic model[16] together with the Degani-Schiff modification[17,18] is used in the present computations. This is an efficient isotropic eddy viscosity model that properly accounts for crossflow separation in the presence of strong vortices above the wing. The original unmodified Baldwin-Lomax model often chooses a length scale associated with a vortical flow structure that lies outside the viscous boundary layer. This results in an eddy viscosity that can be one or two orders of magnitude too large, and effectively suppresses all but the most dominant vortex structure. The modified model of Degani and Schiff restricts the choice of length scale to the boundary-layer region in a rational manner and, therefore, gives appropriate values for the eddy viscosity.

Experimental surface-flow patterns[10] indicate that the Reynolds number based on the wing root chord $Re_c = 3.67 \times 10^6$ is sufficiently high that turbulent transition is confined to a very small region near the delta wing apex. The computations therefore assume fully turbulent flow beginning at the apex of the delta wing, i.e., transitional effects are ignored.

Numerical Algorithm

The NSS code integrates Eq. (1) using a diagonal form of the Beam-Warming algorithm[19] due to Pulliam and Chaussee.[20] This implicit, approximately-factored, central-difference algorithm is second-order-accurate in space and first-order-accurate in time. A combination of second-fourth-order artificial dissipation is used to damp high-frequency errors. The dissipation is automatically reduced within a boundary layer by scaling the dissipation terms with the square of the local fluid speed.[21] A cutoff switch prevents the dissipation from getting too small near solid surfaces. The diagonal algorithm is advanced in time using a scalar pentadiagonal solver. This is computationally more efficient than other methods that utilize block tridiagonal solvers, e.g., the Beam-Warming algorithm.

The spatial accuracy of the NSS code, and zonal grid capability for treating complex geometries has been previously demonstrated by simulating steady transonic viscous flow about the complete F-16A fighter aircraft.[22] The time-accuracy of the algorithm has been demonstrated by computing transonic flow over a wing oscillating in angle of attack.[23] More recently, the accuracy and efficiency of the NSS code[21] was demonstrated by computing high-incidence vortical flow about a tangent-ogive cylinder body. Each of these computations compared well with experimental data.

Computational Grids

A three-dimensional hyperbolic method[24] was used to generate a spherical grid for the delta-wing geometry. A perspective view of the wing surface grid and a portion of the sting is shown in Fig. 2. Surface details are resolved by using sufficient grid point clustering. The sting extends behind the wing with a diameter equal to that of the fuselage, i.e., the reduced diameter of the experimental test rig was not modeled. A portion of the viscous grid clustering is shown in the

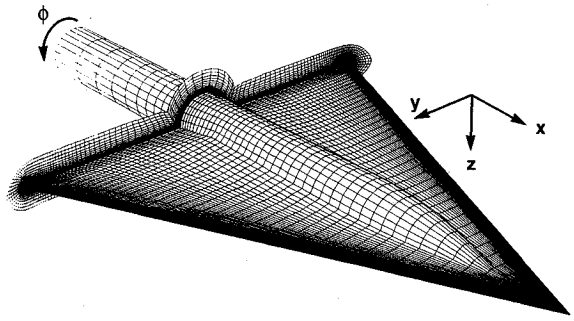

Fig. 2 Perspective view of computational grid.

figure at the wing trailing edge. The spherical axis extends upwind from the wing apex. The far-field boundaries (not shown in the figure) extend two chord lengths upwind and downwind of the wing body, and five chord lengths in the body-normal direction. Two grids were generated. A fine grid consisted of 97 points in the streamwise direction, 248 points in the circumferential direction, and 59 points in the body-normal direction, totaling about 1,400,000 grid points. A medium-size grid (shown in Fig. 2) was constructed with 67 points in the streamwise direction, 208 points in the circumferential direction, and 49 points in the body-normal direction, totaling about 700,000 grid points. There are more grid points on the leeward side of the wing (in the circumferential direction) than the windward side to resolve the off-surface vortices while keeping the grid size to a minimum.

A two zone version of the medium-size grid was obtained by splitting the grid in the streamwise direction at approximately 84% of the wing root chord. There are two grid cells of overlap such that both zones share three identical grid surfaces in the streamwise direction.

Numerical Boundary Conditions

The no-slip condition (zero velocity relative to a solid surface) is imposed on the wing and fuselage/sting surfaces, whereas density and pressure are found by extrapolation. The total energy per unit volume is then computed from the perfect gas law. Uniform flow is imposed at the far field, whereas a zero-gradient condition is used at the outflow boundary. Flow variables are averaged across the wake cut that extends from the wing trailing edge downwind to the outflow boundary. Boundary conditions are imposed on the spherical axis by averaging flow variables (one grid point off the axis) in the circumferential direction.

Zonal boundary conditions for the two-zone medium grid are updated sequentially with the most recent data available. Since the grids have coincident surfaces with identical grid points, data transfer from one grid to another is accomplished by direct injection. A more complete description of the zonal interface boundary conditions is given in Ref. 22.

Results

The time-dependent RANS equations are numerically integrated using the NSS code to simulate high-incidence vortical flow about a 65-deg sweep delta wing. The computations presented below include several static (fixed) roll angle cases and one dynamic (forced periodic) roll oscillation case. The flow conditions are freestream Mach number $M_\infty = 0.27$, angle of attack $\alpha = 15$ deg, and Reynolds number based on the wing root chord $Re_c = 3.67 \times 10^6$. The results presented below are compared with experimental wind-tunnel data provided by Hanff.[10]

Static Roll Cases

Static roll computations were obtained by initializing the flowfield with freestream conditions (impulsive start), and using a spatially varying time step to accelerate convergence to a steady state. Once the solution had developed sufficiently, a constant nondimensional time step, $\Delta\tau = 0.005$, was used in case the flow was nonsteady.

Figure 3 compares the computed surface-pressure coefficients C_p with experiment for the fine 97 × 248 × 59, and medium 67 × 208 × 49, grids at zero roll angle, and at the 75% root chord position. A positive semispan coordinate Y is directed outward from the body center towards the right wing leading edge (pilots view) (see Fig. 2). The computed and experimental C_p are in very good agreement with each other for both grids, and are symmetric with respect to the body centerline. Notice there are primary and secondary vortex suction peaks. The primary suction peak is more inboard than the secondary one. The fine grid secondary vortex has a slightly higher suction peak than the medium grid secondary vortex, and is flattened somewhat because it lies directly over

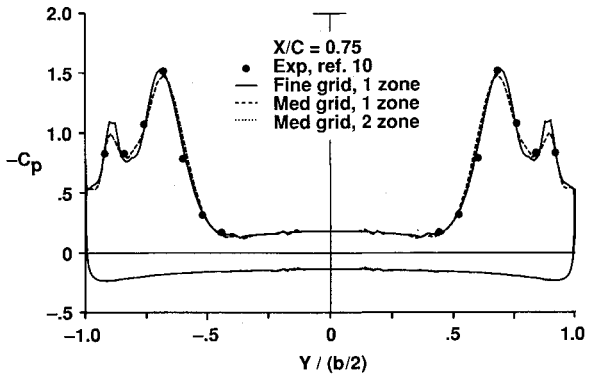

Fig. 3 Effects of grid refinement and zonal boundary condition treatment on the pressure coefficients. $M_\infty = 0.27$, $\alpha = 15$ deg, $Re_c = 3.67 \times 10^6$, $\phi = 0$ deg.

the leading-edge bevel. The C_p distribution for a two-zone medium grid is also shown in Fig. 3. The medium grid was split into two streamwise zones at approximately 84% root chord. This was done to take full advantage of two Cray Y-MP machines that had different memory configurations. The single- and two-zone medium grids have virtually identical C_p. Since the two-zone medium grid gives very good results at half the computational cost of the single fine grid, it is used for all of the remaining static and dynamic cases presented below.

Computations for several different static roll angles, $\phi = 0, -14, -28$, and -42 deg, were investigated to assess their effects on the vortex aerodynamics and solution accuracy. A positive roll angle (see Fig. 2), corresponds to a clockwise rotation about the longitudinal axis such that the right wing moves down and the left wing moves up as viewed from behind the wing (pilot view).

Figure 4 shows helicity-density contours, which are used to visualize the leeward-side vortices at the 75% root chord position. Helicity-density is defined as the dot product of the local velocity and vorticity vectors ($V \cdot \Omega$). A large number of closely spaced contours indicates high vorticity, and hence a strong vortex, whereas a few sparsely spaced contours indicate a weaker vortex. The sign of helicity density indicates the sense of vortex rotation. The cross-sectional views shown in Fig. 4 lie on a plane perpendicular to the body's longitudinal axis. The dotted contours correspond to a clockwise vortex rotation (pilot view), whereas solid line contours correspond to a counterclockwise rotation. Notice there are primary, secondary, and tertiary vortices. Computed[25] and experimental[10] surface-flow patterns also indicates the same vortical flow structure. Notice also that as the right wing moves up (statically), the primary vortex on the right wing grows weaker (fewer contours) and moves outboard, closer to the wing leading edge. This occurs because the leeward wing has an increase in its effective sweep due to roll. The converse is true on the left wing as its wing moves down, i.e., the primary vortex grows stronger and moves inboard towards the fuselage. However, beyond $\phi = -28$ deg, a second mechanism, namely, the reduction of the local angle of attack with roll angle, causes the left primary vortex to weaken somewhat, see $\phi = -42$ deg. Vertical movement of the primary vortices are very slight. All of these trends were observed experimentally[10] and confirm the qualitative nature of the computations.

The right wing consistently has a simple primary, secondary, and tertiary vortex system, whereas the left side develops a double primary/secondary system with a tertiary vortex as the roll angle increases negatively. The latter vortex structure has been observed experimentally[26,27] and computationally[21,28] on slender axisymmetric bodies. A more detailed explanation of the topological and physical significance of this vortical structure can be found in Ref. 21. No vortex breakdown was observed computationally or experimentally[10] under the present flow conditions.

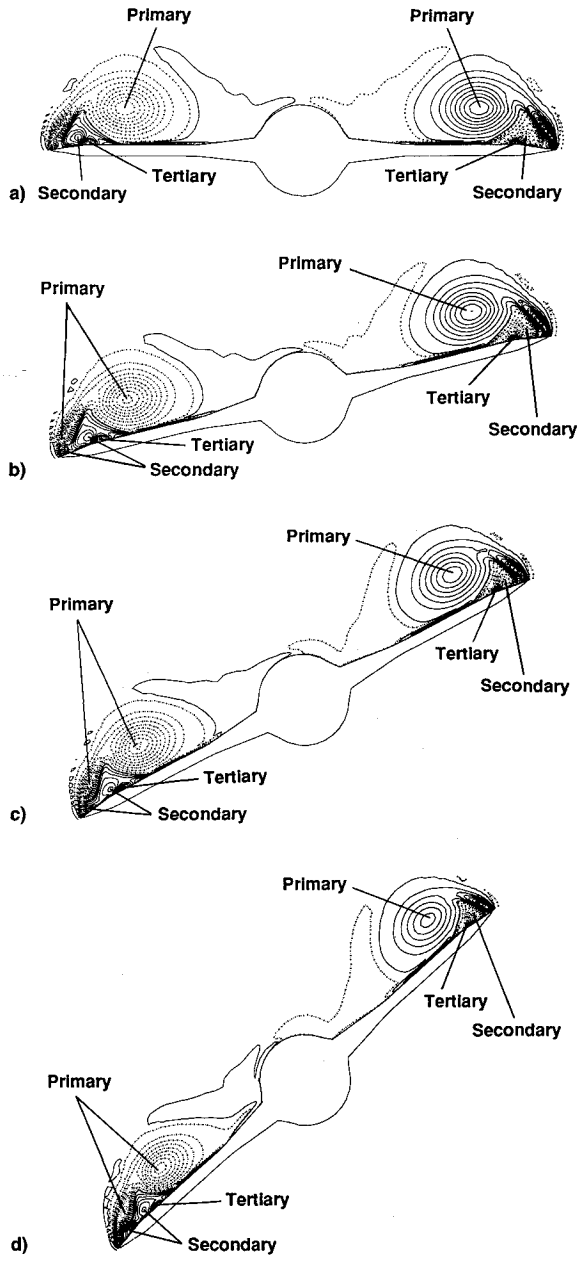

Fig. 4 Helicity-density contours at 75% root chord for different static roll angles. M_∞ = 0.27, α = 15 deg, Re_c = 3.67 × 10⁶. ϕ = a) 0, b) −14, c) −28, and d) −42 deg.

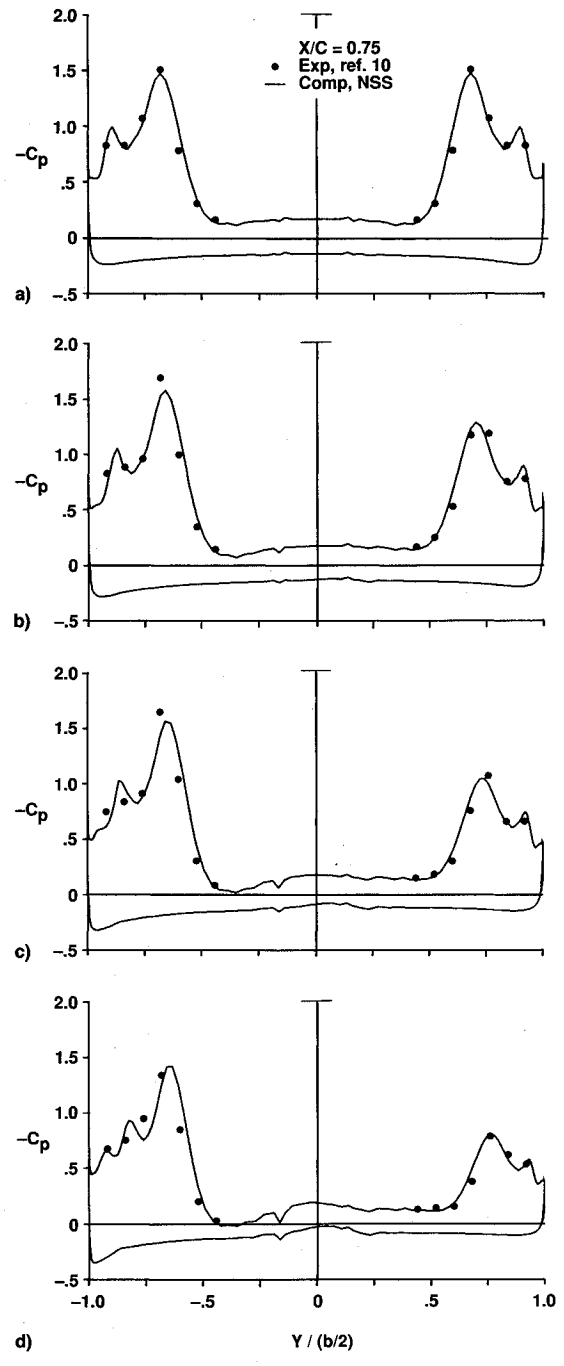

Fig. 5 Comparison of computational and experimental pressure coefficients for different static roll angles. M_∞ = 0.27, α = 15 deg, Re_c = 3.67 × 10⁶. ϕ = a) 0, b) −14, c) −28, and d) −42 deg.

A comparison of computed and experimental C_p is shown in Fig. 5 for the static roll cases. Overall, the quantitative agreement is very good. There is a slight bend in the computed C_p curves in the wing/body juncture region due to grid coarseness. As the roll angle is increased negatively, there is a reduction of the right wing primary suction peaks, and the vortices move closer to the wing leading edge. Conversely, the left wing has increased primary suction peaks (up through ϕ = −28 deg) and inboard vortex movement. This is consistent with the previous helicity-density discussion. Notice also the small secondary suction peaks. These suction peaks correspond precisely with the spanwise location of the secondary vortex cores (cf. Figs. 4 and 5). Although the experimental data[10] is too sparse to definitively indicate this detail, other experimental investigations[29-31] report multiple suction peaks due to primary and secondary vortices on delta wings in the 10–20-deg angle-of-attack range.

The static rolling-moment coefficient C_l is shown as a function of roll angle in Fig. 6. The computational values for positive roll angles were obtained by assuming symmetry with

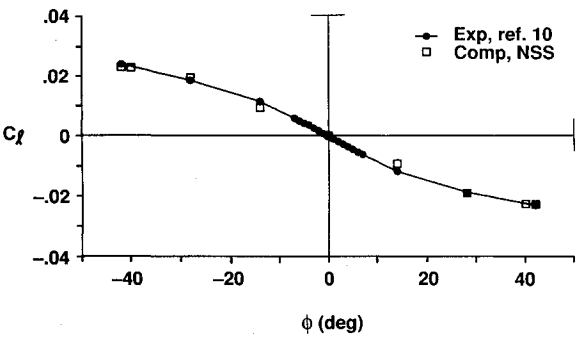

Fig. 6 Comparison of computational and experimental rolling-moment coefficients for different static roll angles. M_∞ = 0.27, α = 15 deg, Re_c = 3.67 × 10⁶.

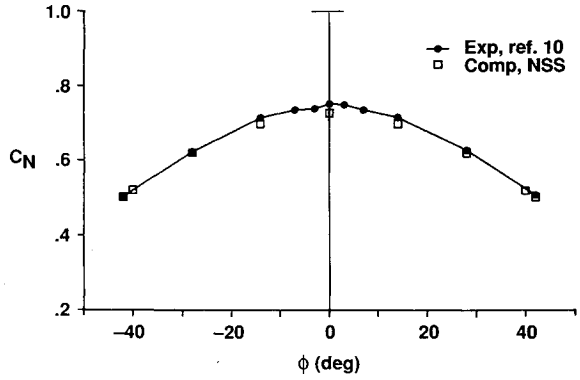

Fig. 7 Comparison of computational and experimental normal-force coefficients for different static roll angles. $M_\infty = 0.27$, $\alpha = 15$ deg, $Re_c = 3.67 \times 10^6$.

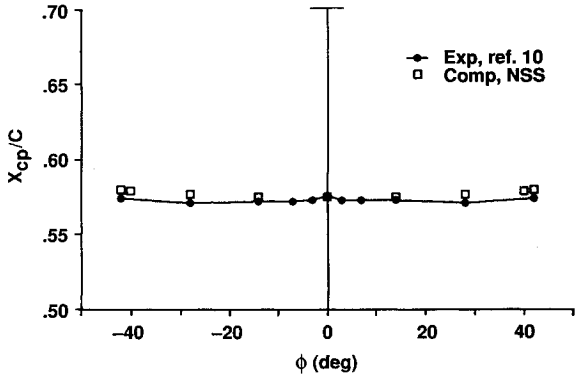

Fig. 8 Comparison of computational and experimental streamwise c.p. locations for different static roll angles. $M_\infty = 0.27$, $\alpha = 15$ deg, $Re_c = 3.67 \times 10^6$.

the negative roll angle results. Experimental values for both positive and negative roll angles are also shown. Agreement between computed and experimental C_l for all roll angles is excellent. The negative slope of the C_l curve indicates a statically stable delta wing with a trim point at zero roll under the present flow conditions. The variation of static normal-force coefficient C_N with roll angle is shown in Fig. 7. Once again the agreement between computation and experiment is excellent throughout the roll angle range, indicating the proper lift is captured. The variation of streamwise c.p. X_{CP}/C with roll angle is approximately constant and is shown in Fig. 8. The agreement between computation and experiment is very good, indicating the proper pitching moment is captured.

Overall, there was very good agreement, qualitatively and quantitatively, between computation and experiment over a large range of static roll angles spanning $-42 \leq \phi \leq 42$ deg. All of the anticipated trends were predicted. The NSS code required 17 μ-s/grid point/time step on a Cray Y-MP. A static solution using the medium-size grid typically required about 8000 steps to converge from an impulsive start. This corresponds to about 26 h of Cray Y-MP time per static case.

Dynamic Roll Oscillation

The NSS code was used to compute the flowfield about the 65-deg sweep delta wing that was forced to roll about its longitudinal axis according to

$$\phi(t) = -\Phi_{max} \cos(\omega t) \tag{2}$$

where the amplitude of motion is $\Phi_{max} = 40$ deg, the circular frequency $\omega = 44$ rad/s ($f = 7$ Hz), and t is the time variable in seconds. The reduced frequency is given by

$$k = (\omega b/2V_\infty) = 0.14 \tag{3}$$

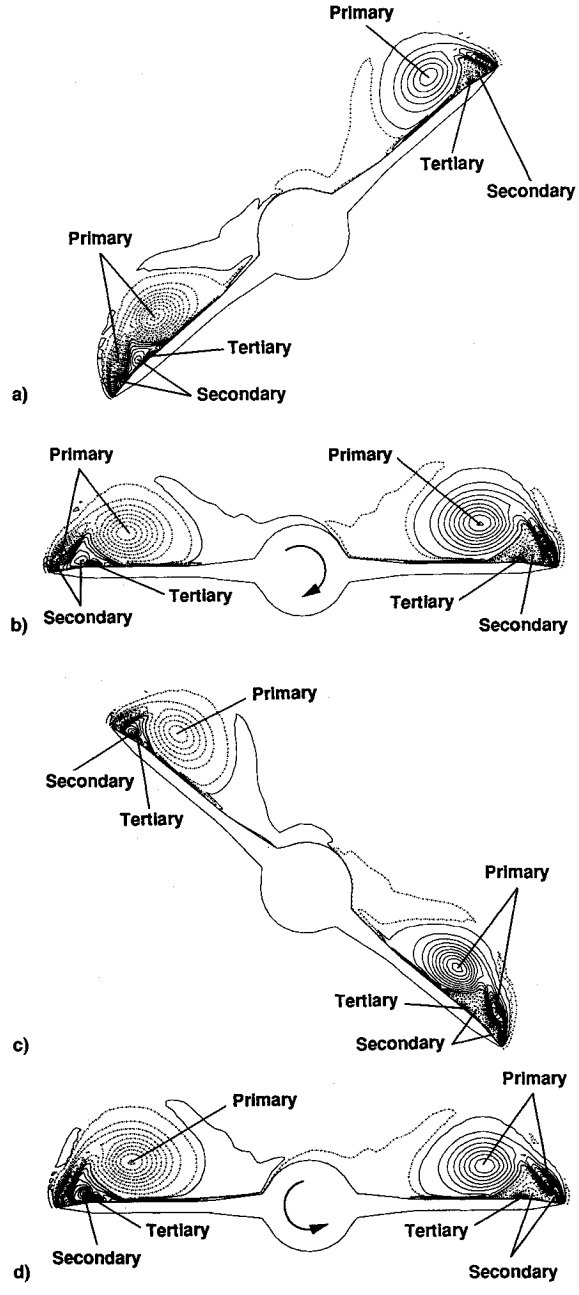

Fig. 9 Dynamic helicity-density contours at 75% root chord and four sequential roll angle positions. $M_\infty = 0.27$, $\alpha = 15$ deg, $Re_c = 3.67 \times 10^6$, $\Phi_{max} = 40$ deg, $k = 0.14$. ϕ = a) -40, b) 0, c) 40, and d) 0 deg.

where b is the span of the delta wing, and V_∞ is the freestream speed. The freestream conditions are the same as the static roll cases, i.e., $M_\infty = 0.27$, $\alpha = 15$ deg, and $Re_c = 3.67 \times 10^6$. The direction of positive roll is indicated in Fig. 2.

There were 15,000 time steps per cycle, which corresponds to a nondimensional time step of $\Delta\tau = 0.005$. According to Eq. (2), the roll oscillation at $\phi = -40$ deg has zero angular velocity. Consequently, a static case with $\phi = -40$ deg was first computed and used as the initial condition for the dynamic case. This "smooth" start minimizes the initial transients and achieves a periodic state as rapidly as possible. The numerical and experimental results presented below have reached their periodic states.

Figure 9 shows instantaneous helicity-density contours at 75% root chord and four sequential roll orientations, i.e., $\phi = -40$ deg ($\dot{\phi} = 0$), $\phi = 0$ deg ($\dot{\phi} > 0$), $\phi = 40$ deg ($\dot{\phi} = 0$), and $\phi = 0$ deg ($\dot{\phi} < 0$). When $\dot{\phi} > 0$, the body is rotating in a clockwise direction as viewed from behind the

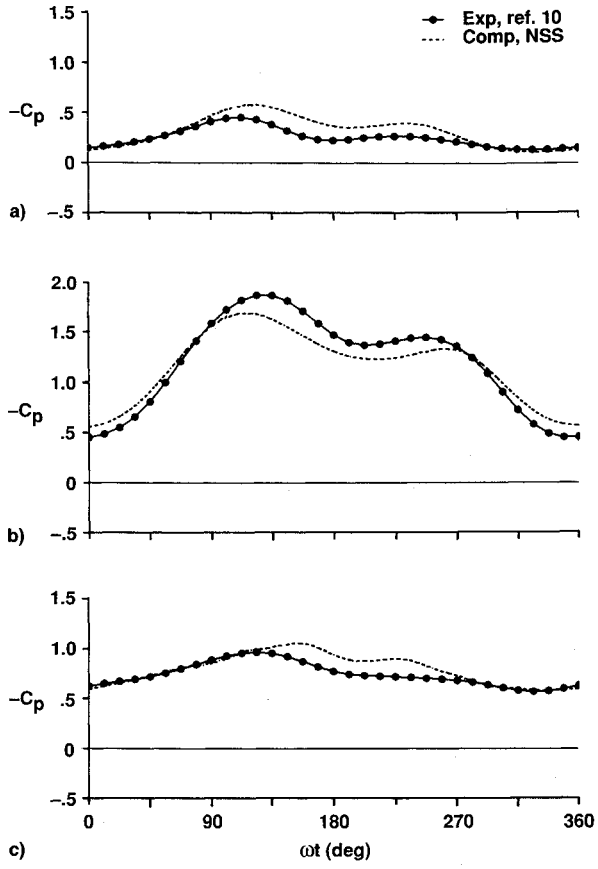

Fig. 10 Comparison of computational and experimental time-dependent pressure coefficients at 75% root chord. $M_\infty = 0.27$, $\alpha = 15$ deg, $Re_c = 3.67 \times 10^6$, $\Phi_{max} = 40$ deg, $k = 0.14$. $Y/(b/2)$ = a) 0.52, b) 0.68, and c) 0.84.

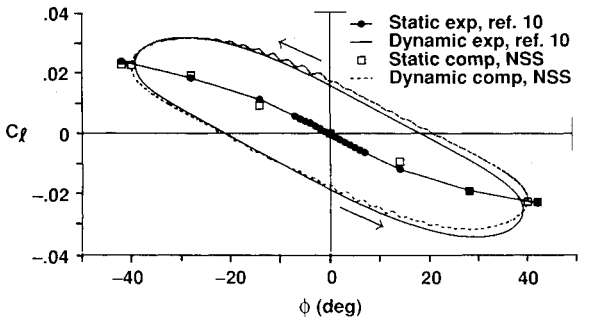

Fig. 11 Comparison of computational and experimental rolling-moment coefficients for dynamic and static cases. $M_\infty = 0.27$, $\alpha = 15$ deg, $Re_c = 3.67 \times 10^6$, $\Phi_{max} = 40$ deg, $k = 0.14$.

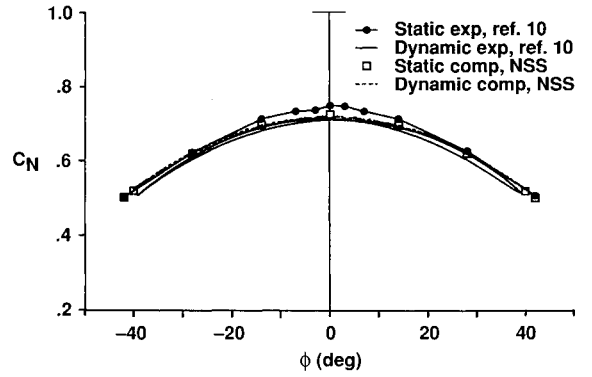

Fig. 12 Comparison of computational and experimental normal-force coefficients for dynamic and static cases. $M_\infty = 0.27$, $\alpha = 15$ deg, $Re_c = 3.67 \times 10^6$, $\Phi_{max} = 40$ deg, $k = 0.14$.

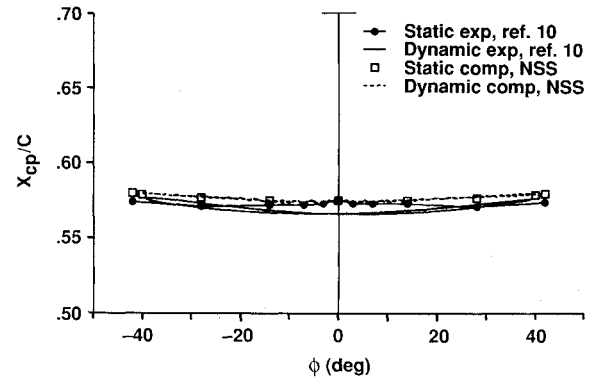

Fig. 13 Comparison of computational and experimental streamwise c.p. locations for dynamic and static cases. $M_\infty = 0.27$, $\alpha = 15$ deg, $Re_c = 3.67 \times 10^6$, $\Phi_{max} = 40$ deg, $k = 0.14$.

wing (pilot view). The solid contours again indicate a counterclockwise rotation, and the dotted contours indicate a clockwise rotation. The dynamic vortex structures and strengths for $\phi = \pm 40$ deg are very similar to the static case when $\phi = -42$ deg (cf. Figs. 9a and 9c with Fig. 4d). However, the static and dynamic cases are quite different at zero roll angle. Figure 9b ($\phi = 0$ deg, clockwise rotation) and Fig. 9d ($\phi = 0$ deg, counterclockwise rotation) indicate vortex asymmetries. The static case, when $\phi = 0$ deg, is of course symmetric. When the body is rotating clockwise, the right wing primary vortex is stronger and higher than on the left wing. This is consistent with the increased local angle of attack on the right wing, and the decreased local angle of attack on the left wing. The converse is true when the body is rotating counterclockwise. There was no vortex breakdown along the wing in either the computations or experiment.

Time histories of computed and experimental pressure coefficients are shown in Fig. 10. These comparisons correspond to a 75% root chord position and three semispan locations on the right wing, i.e., $Y/(b/2) = 0.52$, 0.68, and 0.84. The computed and experimental C_p compare well with each other, even at $Y/(b/2) = 0.68$, where changes in the primary vortex position and strength cause a pressure coefficient change of 1.5.

Figure 11 shows a comparison of the computed and experimental dynamic rolling-moment coefficients as a function of roll angle. The time history of these curves follows a counterclockwise direction (as indicated by the arrows). The computed and experimental C_l compare very well with each other and have essentially the same shape. Static C_l are also shown in the figure. Notice that the static and dynamic C_l are very near each other at the extreme roll angle positions, $\phi = \pm 40$ deg, but differ substantially from each other at zero roll angle. These differences are due to rate-induced time-history effects, where the body passes through its largest angular velocity. Therefore, under the present flow conditions, time-history effects appear to be small at the extreme roll angle positions and quite significant elsewhere.

Both the first and second computed cycles are shown in Fig. 11. They are essentially identical, i.e., there were no significant initial transients. This fortuitous behavior was due to the smooth start procedure described above, and the fact that the static and dynamic C_l are very close to each other at the extreme roll angles, $\phi = \pm 40$ deg. This will not be the case in general. For example, vortex breakdown can introduce time-history lags such that the static and dynamic C_l differ substantially from each other at the maximum roll angle positions.

The area enclosed by the C_l vs ϕ curve represents the nondimensional work done by the fluid on the wing per cycle, and is given by

$$\mathcal{W} = \oint C_l \, d\phi \tag{4}$$

The computational value $\mathcal{W}_c = -2.26$ deg, and the experimental value $\mathcal{W}_e = -2.19$ deg agree within 3%. The sign of the work and counterclockwise time history indicate that the fluid is extracting energy from the wing motion, i.e., the wing is positively damped. This wing will not wing rock freely under the present flow conditions. The computational curve indicates a small amplitude, high-frequency perturbation that begins approximately when the body passes through zero roll angle and persists for about 20 deg of motion. This corresponds to when the body passes through its maximum angular rate ($\dot{\phi}_{max} = 1760$ deg/s), and then begins to slow down. This small perturbation is believed to be numerical as halving the time step for one-half of a cycle reduced the amplitude of the oscillation. Nevertheless, the agreement between the present computation and experiment is very good.

The computed and experimental dynamic normal-force coefficients are shown in Fig. 12. The analogous comparison for the dynamic c.p. locations is shown in Fig. 13. The agreement between computation and experiment is very good for both quantities. The static values are also shown and lie very close to the dynamic values, indicating that time-history effects are small for these quantities.

Overall, there was very good quantitative agreement between the computed simulation and experimental measurements for this large-amplitude, high-rate roll motion. The NSS code required 18 μ-s/grid point/time step for a dynamic body motion on a Cray Y-MP. One cycle of motion using 15,000 time steps and the medium grid (700,000 points) required 50 h of computer time.

Conclusions

The time-dependent, three-dimensional, Reynolds-averaged, Navier-Stokes equations were numerically integrated using the NSS code to simulate turbulent vortical flow about a 65-deg sweep delta wing at 15-deg angle of attack. Both static and dynamic roll computations were presented and compared with experimental data.[10]

A grid refinement study at zero roll showed that a medium size grid (about 700,000 points) provided sufficient resolution of the pertinent flow physics. Splitting the grid into two zones in the streamwise direction had no observable effects on the surface pressures.

Computations at several static roll angles, i.e., $\phi = 0, -14, -28$, and -42 deg, were presented. The computed surface-pressure coefficients, normal-force coefficients, rolling-moment coefficients, and streamwise c.p. locations compared very well with the experimental data for all roll angles. Both the computations and experiment indicated no vortex breakdown above the wing.

The NSS code was also used to compute a large-amplitude ($\Phi_{max} = 40$ deg), high-rate ($f = 7$ Hz) forced roll motion. The computed and experimental dynamic surface-pressure coefficients were in good agreement with each other. There was also very good agreement between computed and experimental dynamic rolling-moment coefficients, normal-force coefficients, and streamwise c.p. locations. The computed and experimental rolling-moment curves indicated the fluid was extracting energy from the wing motion, i.e., the wing was positively damped. The computed and experimental damping energies agreed within 3%. The dynamic rolling-moment coefficients exhibited significant rate-induced time-history effects, whereas the time-history effects were small for the normal-force coefficients and c.p. locations. Both computation and experiment indicate no vortex breakdown over the wing for the dynamic case.

Acknowledgments

The author would like to thank Lewis Schiff of NASA Ames Research Center for his many helpful suggestions throughout this investigation, Ernest Hanff of the Canadian Institute of Aerospace Research, Ottawa, Canada, for supplying the experimental data, and Yuval Levy of Stanford University, Stanford, California, for his help in preparing the figures.

References

[1]Baucom, C. M., and Clark, C., "Navy Departure/Spin and Air Combat Maneuvering Evaluation of a National Aeronautics and Space Administration Developed Flight Control System for the F-14," *1985 Report to the Aerospace Profession Twenty-Ninth Symposium Proceedings*, The Society of Experimental Test Pilots, Lancaster, CA, 1985, pp. 162–177 (ISSN 0742-3705).

[2]Nguyen, L. T., Yip, L., and Chambers, J. R., "Self-Induced Wing Rock of Slender Delta Wings," AIAA Paper 81-1983, Aug. 1981.

[3]Levin, D., and Katz, J., "Dynamic Load Measurements with Delta Wings Undergoing Self-Induced Roll Oscillations," *Journal of Aircraft*, Vol. 21, No. 1, 1984, pp. 30–36.

[4]Arena, A. S., Jr., and Nelson, R. C., "The Effect of Asymmetric Vortex Wake Characteristics on a Slender Delta Wing Undergoing Wing Rock Motion," AIAA Paper 89-3348, Aug. 1989.

[5]Arena, A. S., Jr., and Nelson, R. C., "An Experimental Study of the Nonlinear Dynamic Phenomenon Known as Wing Rock," AIAA Paper 90-2812, Aug. 1990.

[6]Morris, S. L., and Ward, D. T., "A Video-Based Experimental Investigation of Wing Rock," AIAA Paper 89-3349, Aug. 1989.

[7]Hanff, E. S., and Jenkins, S. B., "Large-Amplitude High-Rate Roll Experiments on a Delta and Double Delta Wing," AIAA Paper 90-0224, Jan. 1990.

[8]Hanff, E. S., Kapoor, K., Anstey, C. R., and Prini, A., "Large-Amplitude High-Rate Roll Oscillation System for the Measurement of Non-Linear Airloads," AIAA Paper 90-1426, June 1990.

[9]Hanff, E. S., and Huang, X. Z., "Roll-Induced Cross-Loads on a Delta Wing at High Incidence," AIAA Paper 91-3223, Sept. 1991.

[10]Hanff, E. S., private communication, Inst. for Aerospace Research, Ottawa, Ontario, Canada, 1992.

[11]Arena, A. S., Jr., and Nelson, R. C., "Unsteady Surface Pressure Measurements on a Slender Delta Wing Undergoing Limit Cycle Wing Rock," AIAA Paper 91-0434, Jan. 1991.

[12]Lee, E. M., and Batina, J. T., "Conical Euler Methodology for Unsteady Vortical Flows About Rolling Delta Wings," AIAA Paper 91-0730, Jan. 1991.

[13]Kandil, O. A., and Salman, A. A., "Effects of Leading-Edge Flap Oscillation on Unsteady Delta Wing Flow and Rock Control," AIAA Paper 91-1796, June 1991.

[14]Kandil, O. A., and Salman, A. A., "Three-Dimensional Simulation of Slender Delta Wing Rock and Divergence," AIAA Paper 92-0280, Jan. 1992.

[15]Pulliam, T. H., and Steger, J. L., "Implicit Finite Difference Simulations of Three-Dimensional Compressible Flow," *AIAA Journal*, Vol. 18, No. 2, 1980, pp. 159–167.

[16]Baldwin, B. S., and Lomax, H., "Thin Layer Approximation and Algebraic Model for Separated Turbulent Flow," AIAA Paper 78-257, Jan. 1978.

[17]Degani, D., and Schiff, L. B., "Computation of Supersonic Viscous Flows Around Pointed Bodies at Large Incidence," AIAA Paper 83-0034, Jan. 1983.

[18]Degani, D., and Schiff, L. B., "Computation of Turbulent Supersonic Flows Around Pointed Bodies Having Crossflow Separation," *Journal of Computational Physics*, Vol. 66, No. 1, 1986, pp. 173–196.

[19]Beam, R. M., and Warming, R. F., "An Implicit Finite-Difference Algorithm for Hyperbolic Systems in Conservation Law Form," *Journal of Computational Physics*, Vol. 22, No. 1, 1976, pp. 87–110.

[20]Pulliam, T. H., and Chaussee, D. S., "A Diagonal Form of an Implicit Approximate-Factorization Algorithm," *Journal of Computational Physics*, Vol. 39, No. 2, 1981, pp. 347–363.

[21]Chaderjian, N. M., "Comparison of Two Navier-Stokes Codes for Simulating High-Incidence Vortical Flow," *Journal of Aircraft*, Vol. 30, No. 3, 1993, pp. 357–364.

[22]Flores, J., and Chaderjian, N. M., "Zonal Navier-Stokes Methodology for Flow Simulation About a Complete Aircraft," *Journal of Aircraft*, Vol. 27, No. 7, 1990, pp. 583–590.

[23]Chaderjian, N. M., and Guruswamy, G. P., "Transonic Navier-Stokes Computations for an Oscillating Wing Using Zonal Grids," *Journal of Aircraft*, Vol. 29, No. 3, 1992, pp. 326–335.

[24]Steger, J. L., and Rizk, Y. M., "Generation of Three Dimensional Body Fitted Coordinates Using Hyperbolic Partial Differential Equations," NASA TM 86753, June 1985.

[25]Chaderjian, N. M., "Navier-Stokes Prediction of Large-Ampli-

tude Delta-Wing Roll Oscillations Characterizing Wing Rock," *Proceedings of the Atmospheric Flight Mechanics Conference*, AIAA, Washington, D.C., 1992, pp. 265–279 (AIAA Paper 92-4428).

[26]Ward, K., and Katz, J., "The Interaction Between Primary and Secondary Flow Structures in the Lee of an Inclined Body of Revolution," AIAA Paper 89-0143, Jan. 1989.

[27]Pagan, D., and Molton, P., "Basic Experiment on a Supersonic Vortex Flow Around a Missile Body," AIAA Paper 91-0287, Jan. 1991.

[28]Ying, S. X., Schiff, L. B., and Steger, J. L., "A Numerical Study of Three-Dimensional Separated Flow Past a Hemisphere Cylinder," AIAA Paper 87-1207, June 1987.

[29]Hummel, D., "On the Vortex Formation over a Slender Wing at Large Angles of Incidence," *Proceedings of the High Angle of Attack Aerodynamics*, AGARD, Sandefjord, Norway, 1978, pp. 15-1–15-17 (AGARD-CP-247, Paper 15).

[30]Verhaagen, N. G., "An Experimental Investigation of the Vortex Flow over Delta and Double-Delta Wings at Low Speed," *Proceedings of Aerodynamics of Vortical Flows in Three Dimensions*, AGARD, Rotterdam, The Netherlands, 1983, pp. 7-1–7-16 (AGARD-CP-342, Paper 7).

[31]Kjelgaard, S. O., Sellers, W. L., and Weston, R. P., "The Flowfield over a 75 Degree Swept Delta Wing at 20.5 Degrees Angle of Attack," AIAA Paper 86-1775, June 1986.